
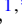





Two-dimensional CP₂ and Li_xCP₂ ($x = 1$ and 2) monolayer with high-mobility transport anisotropy and extraordinary optical properties

Xiaowei Chen ^{1,*}, Jiahe Lin ^{1,*}, Qiubao Lin,¹ Renquan Li,¹ Guanglin Xia ², Weidong Zou ^{1,3} and Xuebin Yu ^{2,†}

¹Department of Physics, School of Science, Jimei University, Xiamen 361021, China

²Department of Materials Science, Fudan University, Shanghai 200433, China

³College of Physics and Electromechanical Engineering, Longyan University, Fujian 364012, China



(Received 30 January 2022; revised 16 July 2022; accepted 19 July 2022; published 2 August 2022)

Two-dimensional CP₂ and Li_xCP₂ ($x = 1$ and 2) monolayers with high-mobility transport anisotropy, and tunable electronic and optical properties were identified through density-functional theory calculations. Our results indicate that the carrier mobility of CP₂ monolayer is highly anisotropic with high hole mobility of $5.192\sim 6.826\text{ m}^2\text{ V}^{-1}\text{ s}^{-1}$ along the x direction. The CP₂ exhibits linear dichroism and extraordinary optical absorption in the ultraviolet- to visible-light spectrum range. More importantly, the electronic and optical properties of CP₂ can be turned via lithiation. A semiconductor to semimetal transition is revealed by lithiated CP₂ with the formation of LiCP₂. The LiCP₂ shows a high Fermi velocity of $0.69 \times 10^6\text{ m/s}$ and strong optical absorbance in midwave-infrared regions. Further increasing the Li concentration leads to a semimetal to direct band-gap semiconductor transition with the formation of Li₂CP₂. The Li₂CP₂ has a high intrinsic conductivity with an anisotropic character (a high electron mobility of $4.665\sim 7.336\text{ m}^2\text{ V}^{-1}\text{ s}^{-1}$ along the y direction) and intense optical absorbance in near-infrared regions. All these desirable properties make CP₂, LiCP₂, and Li₂CP₂ promising for a wide range of future applications in a variety of technologies, especially in electronics, and photovoltaic and optoelectronic devices.

DOI: [10.1103/PhysRevB.106.075402](https://doi.org/10.1103/PhysRevB.106.075402)

I. INTRODUCTION

Two-dimensional (2D) layered materials with intriguing electronic and optical properties have received increasing attention in the past decades. Graphene is one of the typical 2D materials with extremely high carrier mobility of $\sim 10^5\text{ cm}^2\text{ V}^{-1}\text{ s}^{-1}$ at 300 K [1–4], making it a promising candidate for high-performance electronics. The lack of a band gap in graphene, however, limits its applications [5–8]. Few-layer black phosphorus is a new category of layered materials with direct band gap and high carrier mobility, which has a broad application prospect in the field of electronics [9–11].

Previous theoretical works indicate that compared to graphene and black phosphorus alone, the combination of C and P to form a novel 2D carbon phosphide may result in more superior electronic and optical properties due to the competition between the planar sp^2 bonding of C–C and nonplanar sp^3 bonding of P–P [12–17]. For instance, Wang *et al.* reported three allotropes of carbon phosphide, in which the α -CP and β -CP showed superior carrier mobility, while the γ -CP exhibited a semimetallic behavior with Dirac cones [12]. Referring to Guan *et al.*, several allotropes of phosphorus carbide (α_0 -CP, β_0 -CP, α_1 -CP, β_1 -CP, α_2 -CP, and β_2 -CP) were identified, which can be metallic, semimetallic, or direct band-gap semiconductors [13]. Under a sufficiently large strain,

the monolayer carbon phosphide also exhibited extraordinary ability to bend and form ripples with large curvatures [15]. In the study of Yu *et al.*, a new buckled graphenelike C₆P monolayer with extremely high carrier mobility and excellent optical properties was proposed [16]. Additionally, Kar *et al.* reported that CP₃ monolayer with metallic behavior possessed high Fermi velocity on the same order as graphene [17].

Experimental studies on the synthesis of bulk carbon phosphide with P–C bonds were carried out with P-doped diamondlike carbon, radio-frequency plasma deposition with CH₄ and PH₃ gas mixtures [18,19], pulsed laser deposition [20,21], and magnetron sputtering techniques [22]. Theoretical studies suggested that synthesizing CP monolayer via homogeneous doping of C (P) into phosphorene (graphene) and layer exfoliation of three-dimensional (3D) bulk carbon phosphide with β -InS-like structure is possible [14]. Tan *et al.* experimentally confirmed the predicted few-layer α -CP phase through doping C atoms into phosphorene [23,24]. The synthesized α -CP shows high hole mobility of $1995\text{ cm}^2\text{ V}^{-1}\text{ s}^{-1}$, in good agreement with the theoretical calculations.

Although there are many different allotropes of carbon phosphide monolayer that have been reported, it is very possible to find 2D carbon phosphide materials with different stoichiometric compositions or other allotropes due to the diversity of the C–P bond configuration. On the other hand, black phosphorus reacts with Li to form LiP, Li₃P, and other lithium phosphides, resulting in collapse of the layer structure [25]. Our calculation based on crystal orbital Hamilton

*These authors contributed equally to this work.

†yuxuebin@fudan.edu.cn

population (COHP) analysis indicates that compared with P-P bonds in black phosphorus, the carbon phosphide monolayer possesses more stable C-P and C-C bonds, which may result in breaking the relatively weak P-P bonds after lithiation, while preserving the C-C and C-P bonds, thus inducing phase transition to form 2D Li-C-P materials with intriguing electronic and optical properties. As γ -CP has been reported to have strong Li absorption energy [26], we report the phase transition of 2D carbon phosphide induced by lithiation.

Herein, we identified three 2D materials, CP_2 , LiCP_2 , and Li_2CP_2 , with excellent electronic and optical properties. Among them, CP_2 monolayer is a semiconductor with an indirect band gap of 1.14 eV and high hole mobility of $4.665\sim 7.336\text{ m}^2\text{ V}^{-1}\text{ s}^{-1}$, showing excellent optical anisotropy and extraordinary high optical absorbance in the ultraviolet- to visible-light spectrum range. More importantly, the lithiation of CP_2 -induced phase transition and electronic properties changing from indirect band-gap semiconductor to semimetal or direct band-gap semiconductor depends on the concentration of Li. The excellent electronic and optical properties of CP_2 , LiCP_2 , and Li_2CP_2 make them promising candidates for future applications in a wide variety of technologies, particularly for electronic, photovoltaic, and optoelectronic devices.

II. COMPUTATIONAL METHODS

The DFT calculations were performed using a projector-augmented wave [27] method as implemented in MEDEA@VASP [28]. The generalized gradient approximation (GGA) with Perdew-Burke-Ernzerhof [29,30] was applied to describe the exchange-correlation functional. The density-functional dispersion correction (D2-Grimme) [31] was adopted to describe the van der Waals interactions. The plane-wave cutoff energy for wave function was set to 500 eV. A large vacuum distance of $\sim 20\text{ \AA}$ along the z axis was used to minimize the interactions between adjacent layers. Γ -centered k meshes of $16 \times 14 \times 1$ were used to sample the first Brillouin region of the conventional cell for geometric optimization. The shape and volume of the cell were fixed and all atoms in the cell were allowed to relax until the residual force was less than 0.01 eV/\AA . Since GGA usually underestimates the band gap, the hybrid Heyd-Scuseria-Ernzerhof (HSE06) functional [32] was used to get relatively accurate electronic structure and optical properties. The phonon spectra were calculated by the finite displacement method as implemented in the MEDEA@PHONON program [33] with supercell size of $(2 \times 2 \times 1)$, $(2 \times 2 \times 1)$, and $(3 \times 3 \times 1)$ for CP_2 , LiCP_2 , and Li_2CP_2 , respectively. The Li diffusion barriers were estimated by the climbing image nudged elastic band method [34].

The cohesive energies of C_xP_y and Li_zCP_2 were calculated using the following expression:

$$E_c = (E_{\text{total}} - xE_C - yE_P - zE_{\text{Li}})/n,$$

where E_{total} is the total energy of unit cell of C_xP_y or Li_zCP_2 , the E_C , E_P , and E_{Li} are the total energies of a single C, P, and Li atom, respectively; x , y , and z are the number of C, P, and Li atoms in the C_xP_y or Li_zCP_2 unit cell, respectively; n is the number of atoms in the unit cell of C_xP_y or Li_zCP_2 .

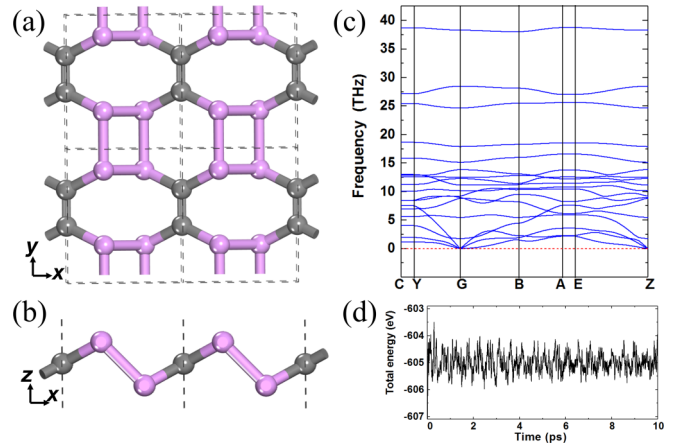


FIG. 1. Top (a) and (b) side views of the monolayer CP_2 sheet with gray balls representing C atoms and pink balls for P atoms. The unit cell is indicated by a gray dashed line. (c) Phonon dispersion relation of the CP_2 monolayer. (d) Evolution of total energy of monolayer CP_2 of AIMD simulations at 300 K.

The low cohesive energy indicates strong binding interactions and the possibility of experimental synthesis from elementary substances.

The formation energies of Li_xCP_2 were calculated using the following expression:

$$E_f = (E'_{\text{total}} - E_{\text{CP}_2} - x\mu_{\text{Li}})/x,$$

where E'_{total} is the total energy of unit cell of Li_xCP_2 ; then, E_{CP_2} is the total energies of CP_2 , μ_{Li} is the chemical potential of Li in lithium metal, and x is the number of Li atoms in the Li_xCP_2 unit cell. The negative formation energy indicates that Li_xCP_2 is energetically more stable than the corresponding CP_2 and Li metal.

Ab initio molecular dynamics (AIMD) simulations were performed using a $4 \times 4 \times 1$ supercell. The canonical ensemble (NVT) following the Born-Oppenheimer implementation was adopted. The ionic equations of motion were integrated using the Nosé-Hoover algorithm with a time step of 1.0 fs. The simulated system was equilibrated at temperatures of 150, 300, and 450 K for 10 ps (10 000 steps). VASP code was used to initial setup for calculations and postprocessing analysis to derive material such as 3D band structure and optical properties from the raw calculated data of VASP code [35]. For chemical bonding analyses, we utilized the COHP method as implemented in the LOBSTER package [36,37].

III. RESULTS AND DISCUSSION

A. Structure of CP_2 and Li_xCP_2

The predicted structure of CP_2 monolayer was shown in Fig. 1 and the lattice constants, bond lengths, and bond angles of CP_2 are summarized in Table I. As shown in Fig. 1(a) and Table I, the CP_2 monolayer has a space group of $P2/m$ and lattice constants of $a = 4.390\text{ \AA}$, $b = 5.166\text{ \AA}$, and $\beta = 89.19^\circ$. The CP_2 monolayer has a puckered surface which is composed of P_4 square connected by P-P bonds and six-membered structure connected by P-P and C-P bonds. Each C atom is surrounded by one C atom and two P atoms. The

TABLE I. Calculated structural parameters of CP₂, LiCP₂, and Li₂CP₂ monolayers.

	a (Å)	b (Å)	β (°)	d_{C-C} (Å)	d_{C-P} (Å)	d_{P-P} (Å)	d_{Li-P} (Å)
CP ₂	4.39	5.17	89.19	1.40	1.81	2.25	
LiCP ₂	4.25	5.11	92.03	1.46	1.79	2.11	2.57
Li ₂ CP ₂	4.26	5.19	90.05	1.44	1.84	2.26	2.54~2.65

average lengths of C–C, C–P, and P–P bonds are 1.40, 1.81, and 2.25 Å, respectively. The P–P bond length in CP₂ is slightly shorter than that in α_1 -PC (2.36 Å), while the C–C and C–P bond lengths are slightly longer than that in α_1 -PC (1.38 and 1.78 Å for C–C and C–P bond, respectively) [13]. Previous theoretical work using the structural searching algorithm based on global optimization method also predicted a CP₂ monolayer [12]. As shown in Fig. 1 and Supplemental Material, Fig. S1 [38], the structure of CP₂ predicted in the present work is different from that in the previous report. The CP₂ monolayer proposed in our work (Fig. 1) has a puckered surface which is composed of P₄ square and C₂P₄ six-membered structure. The previously predicted structure of CP₂ (Fig. S1) is composed of five-membered CP₄ structure and eight-membered C₂P₆ structure. As shown in Table S1, although the structural arrangement of CP₂ proposed in our work is different from that in previous work, the calculated cohesive energies are almost the same. No phonon dispersion or AIMD simulation result of CP₂ was reported in previous work. We performed phonon dispersion calculation and AIMD simulation to confirm the stability of our proposed CP₂ monolayer in the following.

The cohesive energy of CP₂ was also compared with previously reported CP, CP₂, and CP₃ monolayer using the same calculation parameters. As shown in Table S1, the cohesive energies of CP, CP₂, and CP₃ are higher than graphene, but lower than phosphorene depending on their composition. As summarized in Table S1, the cohesive energy of CP₂ is ~0.7 eV higher than that of CP and 0.4 eV lower than that of CP₃. In general, the increased C/P ratio decreases the cohesive energy. In addition, the formation energies of carbon phosphide via reaction of CH₄ and PH₃ were calculated and summarized in Table S2. The formation energy of CP₂ is 0.4 eV higher than that of α -CP and 0.54 eV lower than that of CP₃.

We further performed crystal orbital Hamilton population analyses to study the bonding strength of P–P, C–P, and C–C in CP₂ monolayer. Figure S2 contains the COHP and integrated COHP data of CP₂. The corresponding energy values after integration of COHP up to the Fermi level (ICOHP), an efficient measure of the covalent bond strength, are also shown in Table II and Fig. S2. For comparison, the COHP of CP monolayer, graphene, and monolayer black phosphorus were also calculated and presented in Figs. S3 and S4 [38].

The calculated -ICOHP of P–P in black phosphorus and CP₂ are 5.114 and 5.466 eV, respectively, which are significantly lower than that of C–P (7.382 eV) and C–C (11.987 eV), indicating that P–P bonds are relatively weak compared to that of C–P and C–C bonds. Our calculation also indi-

TABLE II. -ICOHP of P–P, C–P, and C–C.

	P–P	C–P	C–C
Black phosphorus	5.114		
Graphene			11.511
α -CP	4.787	7.572	13.032
CP ₂	5.466	7.382	11.987

cates that the bond strength of P–P is weaker than that of C–P and C–C in previously reported α -CP monolayer. In addition, the energies of breaking the P–P, C–P, and C–C bonds were calculated and summarized in Table S3. The calculated energy of breaking P–P bond is lower than the energy of breaking C–P and C–C bonds, consistent with the ICOHP calculation results.

To examine the dynamic stability of the predicted CP₂ monolayer, we have performed phonon spectra calculations. As shown in Fig. 1(b), no imaginary phonon frequencies exist in the whole Brillouin zone, indicating the inherent dynamical stability of the CP₂ monolayer. In addition, AIMD simulations for 10 ps at 150, 300, and 450 K with a time step of 1 fs were performed using a 4 × 4 × 1 supercell of CP₂. The total energy fluctuation during AIMD simulation and structures after AIMD simulation are shown in Figs. 1(d) and S5. During the AIMD simulations, all the C and P atoms in the supercell are vibrating around their equilibrium positions. Although the slight distortion of six-membered C₂P₄ structure is observed, the C–C, C–P, and P–P bonds are well maintained. Furthermore, the temperature variations of pair-correlation function $g(r)$ were calculated and presented in Fig. S6. The peaks of $g(r)$ are well preserved with increasing AIMD simulation temperature, indicating no phase transition occurs within 10 ps. The above calculation indicates that the CP₂ monolayer has good phase stability at room temperature.

The elastic constants of the CP₂ monolayer were calculated to examine its mechanical stability. The elastic modulus C_{2D} is determined by [39]

$$C_{2D} = \frac{(E - E_0)}{S_0} \times \left(\frac{l_0}{\Delta l} \right)^2,$$

where E_0 and S_0 are the total energy and lattice volume at equilibrium for a 2D system, respectively; E is the total energy of the strain 2D system, l_0 is the lattice constant in the transport direction, and Δl is the deformation of l_0 .

As summarized in Table III, the calculated elastic constants of CP₂ well satisfy the mechanical stability criteria: $C_{11} > 0$, $C_{44} > 0$, and $C_{11} \times C_{22} > C_{12}^2$ [35], demonstrating its mechanical stability. The elastic constants of the CP₂ along the x direction C_{11} is 60.35 J m⁻², significantly higher than that of

TABLE III. Elastic constants of CP₂, LiCP₂, and Li₂CP₂ (in J m⁻²).

	C_{11}	C_{22}	C_{12}	C_{44}
CP ₂	60.35	92.50	21.68	3.39
LiCP ₂	25.26	149.38	14.29	2.37
Li ₂ CP ₂	63.61	128.72	6.84	4.01

28.94 J m⁻² in monolayer black phosphorus [9], which could be attributed to the existence of stronger C–P bonds compared to that of P–P bonds. The elastic constants of the CP₂ along the y direction C_{22} are 92.50 J m⁻², which is slightly lower than that of 101.6 J m⁻² in monolayer black phosphorus.

Since the P–P bonds are relatively weak compared with that of C–P and C–C bonds in CP₂ monolayer, it is intriguing to find out whether the lithiation of CP₂ would lead to cleavage of P–P bonds and induce phase transition from CP₂ to Li–C–P materials with interesting electronic and optical properties. Keeping this in mind, the lithiation of CP₂ with various Li concentration were investigated using $2 \times 2 \times 1$ supercell of CP₂. Our calculations indicate that the P–P bridge sites are the most stable adsorption site for Li. Hence, the number of Li atoms on the P–P bridge sites were gradually increased and the corresponding cohesive energies and structural arrangements are summarized in Tables S4 and S8. As summarized in Table S4, the cohesive energy increased with increasing Li atoms, which indicates that the bond energy of Li–P is lower than that of P–P, C–P, and C–C in CP₂. We further compared the energies of Li_xCP₂ with CP₂ monolayer and Li metal in terms of formation energy. As presented in Fig. S8, our calculated results indicate that the formation energy of Li_xCP₂ reduces with increasing the Li concentration from $x = 0$ to 1. The formation energy of LiCP₂ is almost the same as Li₂CP₂. When the concentration of Li is further increased to $x = 3$, the formation energy is significantly increased to -0.87 eV. Although the negative formation energies indicate that Li_xCP₂ are energetically feasible, the dynamical stability of Li_xCP₂ need to be confirmed by phonon dispersion relation. Various structures of Li_xCP₂ ($x = 0.125 \sim 3$) were examined (Fig. S7), but only the LiCP₂ and Li₂CP₂ show no imaginary phonon frequencies exist in the whole Brillouin zone [Figs. 2(c) and 2(d)], indicating the inherent dynamical stability of the LiCP₂ and Li₂CP₂. The AIMD simulations were performed using $4 \times 4 \times 1$ supercell of LiCP₂ and Li₂CP₂. All the Li, C, and P atoms in the supercell are vibrating around their equilibrium positions during the AIMD simulations; although the distortion of six-membered C₂P₄ structure is observed, the C–C, C–P, and P–P bonds are well maintained (Fig. S9 and Fig. S11). In addition, as shown in Figs. S10 and S12, the peaks of $g(r)$ are well preserved with increasing AIMD simulation temperature, indicating no phase transition occurs within 10 ps. It should be noted that it is still possible to find other allotropes of Li_xCP₂ monolayers using global optimization algorithms.

The LiCP₂ [as shown in Fig. 2(a)] possesses a space group of $P2/M$, and the optimized lattice constants are $a = 4.25$ Å, $b = 5.11$ Å, and $\beta = 92.03^\circ$. The x direction of LiCP₂ is composed of C, P, and Li atoms and the y direction is composed of alternating C–C, P–P dimers and C–P bonds, and Li atom coordinates with neighboring P atoms. The average Li–P bond length is 2.57 Å, which is slightly shorter than that of 2.64 Å in LiP [40]. The structure of Li₂CP₂ has a space group of PM and lattice constants of $a = 4.26$ Å, $b = 5.19$ Å, and $\beta = 90.05^\circ$. The C–C and C–P bonds and other P–P bond lengths are comparable to that of CP₂ monolayer. The shortest Li–Li distance is 2.79 Å, about 0.2 Å longer than LiP, and similar to Li₃P [40]. As shown in Figs. S13 and S14, the calculated -ICOHP of P–P is 7.560 eV, comparable to that

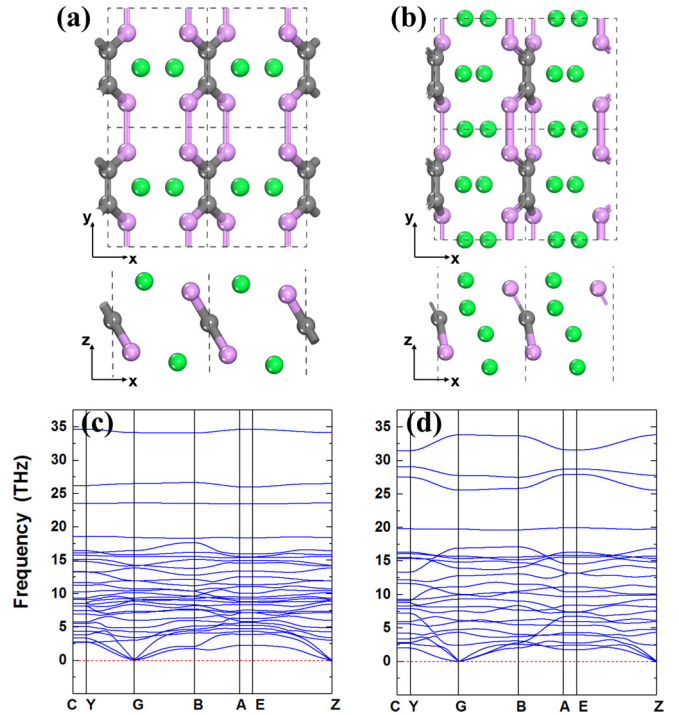


FIG. 2. Top and side views of the monolayer LiCP₂ (a) and Li₂CP₂ (b) with gray balls representing C atoms, pink balls for P atoms, and green balls for Li atoms. The unit cell is indicated by a gray dashed line. Phonon dispersion relation of the (c) LiCP₂ and (d) Li₂CP₂ monolayer.

of C–P (7.589 eV), indicating the similar bonding strength of P–P and C–P in LiCP₂ monolayer. In the case of Li₂CP₂, according to the ICOHP values, the bonding strength is C–C > C–P > P–P. As summarized in Table III, the calculated elastic constants of the LiCP₂ and Li₂CP₂ well satisfy the mechanical stability criteria: $C_{11} > 0$, $C_{44} > 0$, and $C_{11} \times C_{22} > C_{12}^2$ [35], demonstrating their mechanical stability. The elastic constants calculation reveals that LiCP₂ has a low C_{11} of 25.26 J m⁻² due to its unique structure. As shown in Fig. 2(a), the x direction of LiCP₂ is composed of C, P, and Li atoms. Hence, applied external strains along the x direction need to overcome relatively weak Li–P ionic bonds. Compared with LiCP₂, the increased Li–P bonds in Li₂CP₂ result in increasing the C_{11} to 63.61 J m⁻². The y direction of both LiCP₂ and Li₂CP₂ are composed of alternating P–P, C–P, and C–C bonds, which show relatively high C_{22} of 149.38 and 128.72 J m⁻², respectively.

We also examined the formation energies and structure stability of Na_xCP₂ and K_xCP₂. Our preliminary calculation indicates that both the Na_xCP₂ and K_xCP₂ have negative formation energies. As shown in Fig. S15, imaginary phonon frequencies were found for NaCP₂, which indicates that NaCP₂ is dynamically unstable. Figure S16 shows that no imaginary phonon frequency exists in the whole Brillouin zone of KCP₂, indicating the inherent dynamical stability of the KCP₂ monolayer. The structural arrangement and mechanical properties of KCP₂ are included in Fig. S17 and Table S5. As summarized in Table 5, the calculated elastic constants of KCP₂ well satisfy the mechanical stability

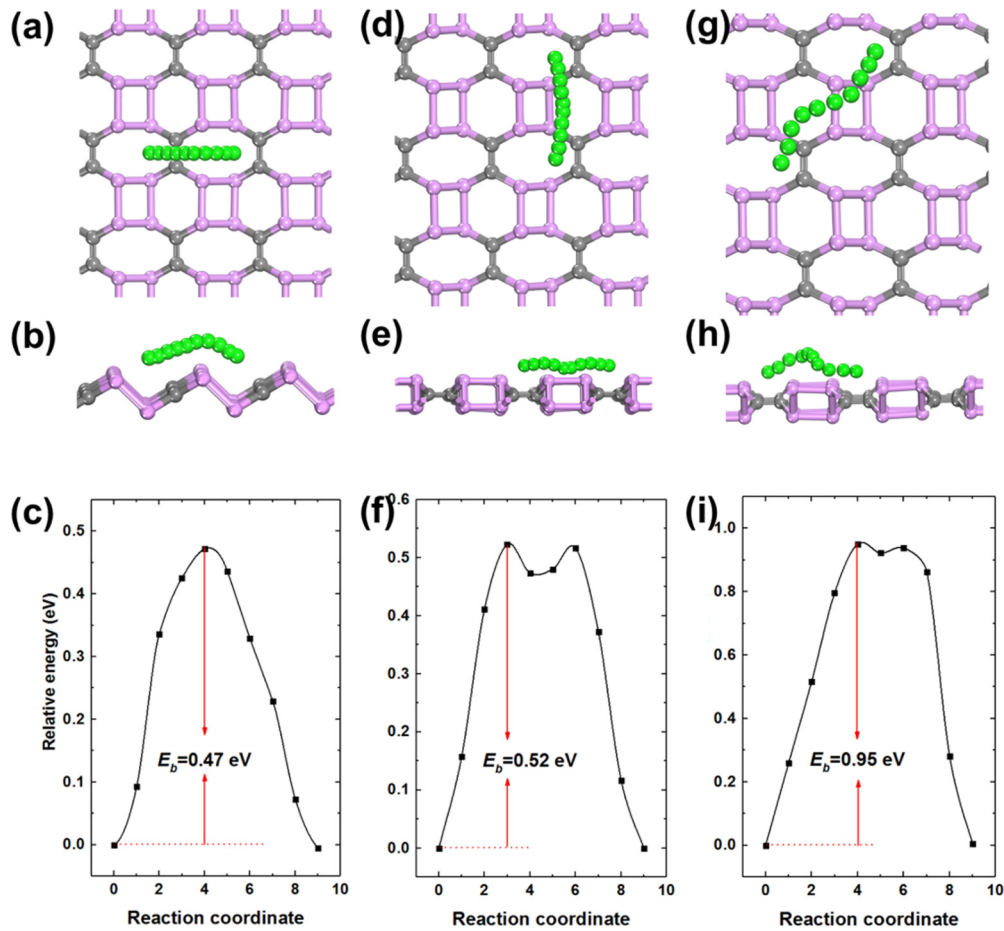


FIG. 3. Top view (a), (d), (g) and side view (b), (e), (h) of the diffusion pathway of Li on CP₂ surface. The green balls represent the diffusion of Li. (c), (f), (i) represent the diffusion-energy barriers.

criteria: $C_{11} > 0$, $C_{11} \times C_{22} > C_{12} \times C_{12}$, and $\det(C_{ij}) > 0$, demonstrating its mechanical stability. The elastic constants of the KCP₂ along the x direction C_{11} are 50.298 J m^{-2} , significantly higher than that of 25.26 J m^{-2} in monolayer CP₂. In addition, the elastic constant of the KCP₂ along the y direction is comparable to that along the x direction, which is due to the similar structural arrangement along the x - and y directions. We would like to focus on the Li_xCP₂ in this paper, and the structural stability and electronic properties of Na_xCP₂ and K_xCP₂ will be discussed in detail in the future.

The above calculation results suggest that lithiation of CP₂ monolayer leads to the formation of structures of LiCP₂ and Li₂CP₂. To further understand the phase transition from CP₂ to LiCP₂ and Li₂CP₂, the diffusion path and energy barrier of Li on the CP₂ and Li₂CP₂ monolayer were investigated. Our calculations indicate that the P-P bridge sites are the most stable adsorption site for Li. Hence, the diffusion of Li from one P-P bridge site to the three nearest P-P bridge sites were studied. As shown in Figs. 3(a)–3(c) and 3(d)–3(f), single Li atoms diffuse along the x - and y directions to the next P-P bridge site and need to overcome relatively low-energy barrier of 0.47 and 0.52 eV, respectively. The energy barrier of Li diffused along the diagonal direction [Figs. 3(g)–3(i)] is significantly higher than that along the x - and y directions, indicating that Li prefers to diffuse along the x - and y direction. The calculated energy barrier for a single Li atom

diffused on the CP₂ monolayer is about 0.3 eV lower than that of Li diffused on phosphorene monolayer (0.76 eV) [41], which indicates that the diffusion of Li is preferable on the CP₂ monolayer. In order to study the diffusion of Li on the Li₂CP₂, a Li vacancy was created and the energy barrier for the diffusion of a neighboring Li atom towards the Li vacancy was calculated. As shown in Fig. 4, the energy barrier of a Li atom diffuses along x , y and the diagonal directions are 0.51, 0.91, and 1.68 eV, respectively. This indicates that Li prefers to diffuse along the x direction on the Li₂CP₂. It has been reported that the Li diffusion energy barrier increases with increasing Li concentration on the monolayer black phosphorene [41]. In contrast, the energy barrier of Li diffused along the x direction on the Li₂CP₂ is very close to that of CP₂, suggesting the diffusion of Li is preferable on both the CP₂ and Li₂CP₂ monolayers.

B. Electronic structures

Since GGA usually underestimates the band gap, the hybrid HSE06 functional form was used to obtain accurate electronic properties. Figure 5 presents the band structure, electron localization function (ELF), and density of states (DOS) of the CP₂ calculated with the HSE06 functional. As shown in Figs. 5(a) and 5(b), the CP₂ is a semiconductor with an indirect band gap of 1.14 eV, which is 0.37 eV lower than

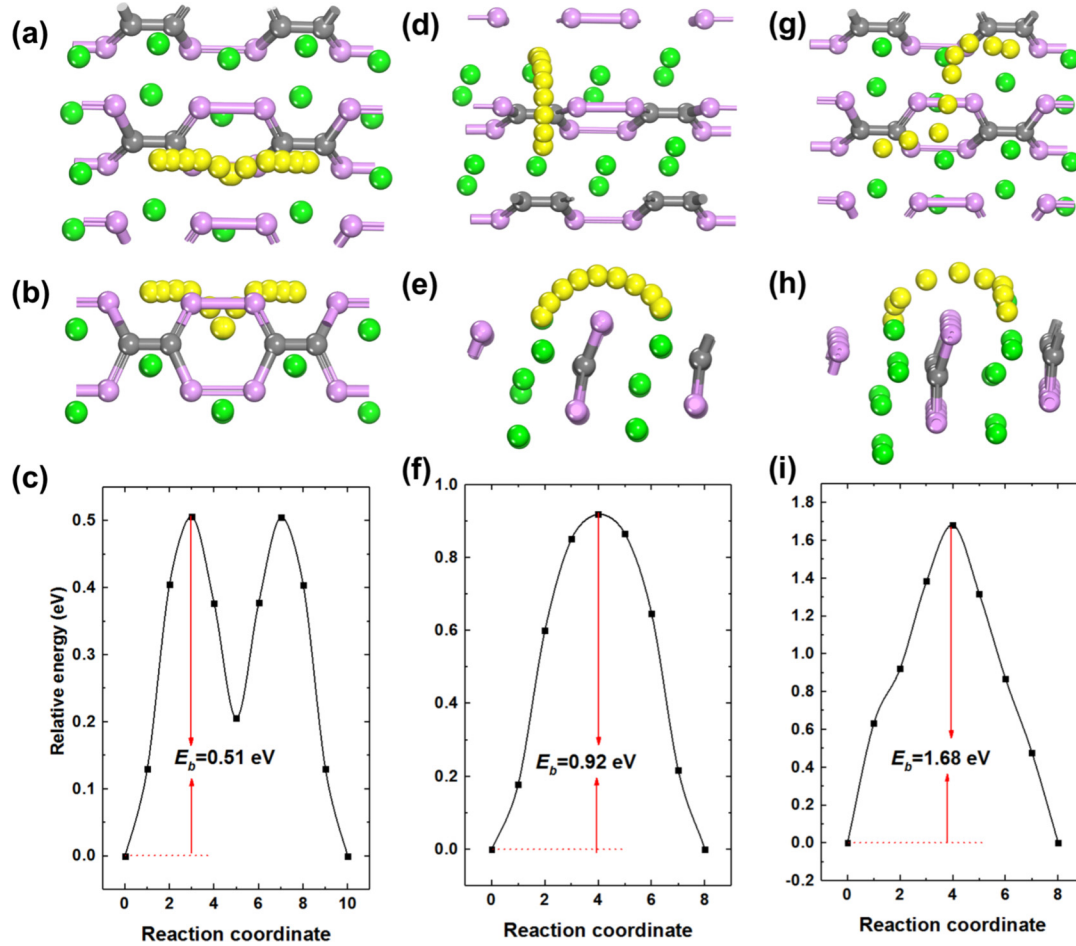


FIG. 4. Top view (a), (d), (g) and side view (b), (e), (h) of the diffusion pathway of Li on Li_2CP_2 surface. The yellow balls represent the diffusion of Li. (c), (f), (i) represent the diffusion-energy barriers.

that of monolayer black phosphorus [9]. The valence-band maximum (VBM) and the conduction-band minimum (CBM) are located at (0.5000, 0.3668, 0.0000) and (0.2835, 0.5000, 0.0000) in reciprocal space, respectively. The ELF results as shown in Figs. 5(c) and S18 indicate that the C–C bonds are in the sp^2 configuration, similar to that in graphene. There is a nonbonding lone electron pair around each P atom. The P atoms adopt sp^3 hybridization configuration, in which one of the hybrid orbitals is filled with a lone electron pair, and the other three hybrid orbitals form covalent bonds with the neighboring C and P atoms. The DOS [see Fig. 5(d)] reveals that the VBM and CBM of the CP_2 monolayer are predominantly derived from the p orbitals of C and P atoms.

It should be noted that the projected band structure of LiCP_2 shows two quasi-Dirac cones around the Fermi level [see Fig. 6(a)], indicating that the lithium of CP_2 induces the transition of electronic properties from semiconductor to semimetal. The VBM and CBM are located at (0.0000, 0.2051, 0.0000) and (0.5000, 0.2051, 0.0000) in reciprocal space, respectively. The calculated 3D band structure of LiCP_2 [see Fig. 6(b)] further confirmed that the quasi-Dirac cones are not caused by band fold, which means that LiCP_2 would have great potential on high-efficiency photoelectric detectors. By a linear fitting of the band, we obtain the Fermi velocity $v_F = \frac{1}{\hbar} \left(\frac{\partial E_k}{\partial k} \right)_{E_k=E_f}$ of the Dirac fermions in LiCP_2 .

The Fermi velocity is 0.69×10^6 m/s along the k_y direction, which is very close to that of graphene (0.85×10^6 m/s) [42]. The Fermi velocity is 0.16×10^6 m/s along the k_x direction. Both the high- and direction-dependent Fermi velocities imply the great potential for direction-dependent quantum information devices. The ELF results [Figs. 6(c), 7(c), S19, and S20] indicate that for both LiCP_2 and Li_2CP_2 , the C–C covalent bonds are in the sp^2 configuration, and the C–P and P–P covalent bonds are in the sp^3 configuration, similar to that of CP_2 . The ELF between Li and P is close to zero, indicating the ionic bonds feature of Li–P. It is observed from the DOS of LiCP_2 [as shown in Fig. 6(d)] that the densities of states near the VBM and CBM have significant contributions from the p orbitals of C and P, while the contributions from Li atoms are much lower. The densities of states close to the VBM and CBM are relatively high, indicating strong optical absorption may be observed in the infrared region.

As mentioned above, a further increase in the concentration of Li results in the formation of Li_2CP_2 . The electronic properties of Li_2CP_2 are distinct from that of LiCP_2 and CP_2 . As shown in Figs. 7(a) and 7(b), the Li_2CP_2 is a semiconductor with a direct band gap of 0.88 eV. The VBM and CBM are located at (0.0000, 0.5, 0.0000) in reciprocal space. The partial DOS of the Li_2CP_2 monolayer [Fig. 7(d)] reveals that the states near the VBM and CBM are predominantly derived

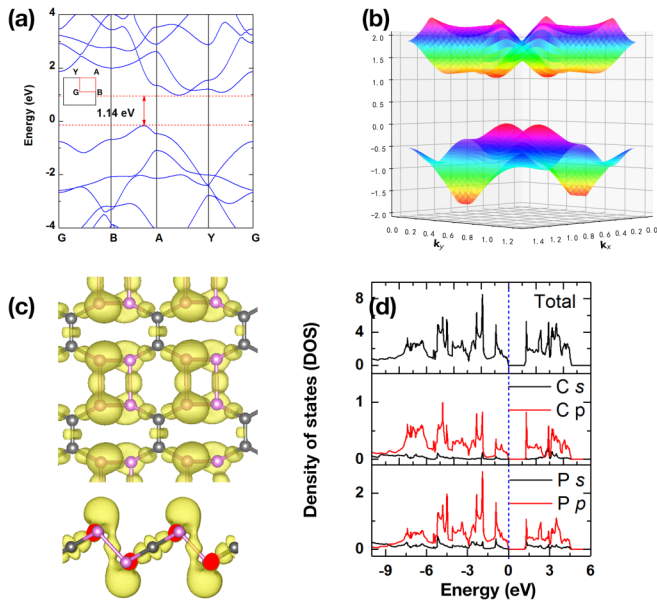


FIG. 5. Electronic properties of CP₂ monolayer: (a) Projected band structure with Brillouin-zone inset; (b) three-dimensional band structures of the highest valence band and lowest conduction band; (c) ELF with isosurface value set to 0.8; and (d) total DOS of CP₂, along with orbital projection for *p* and *s* orbitals of C and P.

from the *p* orbitals of C, P, and Li. It has been reported that the adsorption of Li on the monolayer black phosphorus surface leads to electronic properties change from semiconductor to metal [41]. Unlike single-layer black phosphorus, CP₂ has tunable electronic properties that convert it from an indirect band-gap semiconductor (CP₂) to a semimetal (LiCP₂) and then to a direct band-gap semiconductor (Li₂CP₂) depending on the concentration of Li.

C. Effective mass and carrier mobility

The finite-difference method was used to estimate the effective mass of CP₂ and Li₂CP₂ [43]. The effective mass of holes in CP₂ along different directions at VBM [(0.5000, 0.3585, 0.0000) in reciprocal space] and the effective mass of electrons along different directions at CBM [(0.2835, 0.5000, 0.0000) in reciprocal space] were estimated and presented in Fig. 8. The effective mass of electrons is significantly greater along the *x* direction than along the *y* direction. The electrons have the smallest effective masses of 0.12 *m*₀ at the *y* direction. The electrons' effective mass reach a maximum of 0.47 *m*₀ along the *x* direction. In addition, the effective masses of holes in CP₂ are asymmetric in the *y* direction, consistent with the asymmetric energy band structure as shown in Fig. 2(b). The holes have the smallest effective mass of 0.21 *m*₀ along *y* direction and reach a maximum of 0.43 *m*₀ along the *x* direction.

The effective mass of electrons and holes in Li₂CP₂ along different directions at CBM and VBM [(0.5000, 0.3585, 0.0000) in reciprocal space] are estimated. As presented in Fig. 8(b), the Li₂CP₂ shows high anisotropy in effective mass of electrons, namely 1.47 *m*₀ and 0.21 *m*₀ along the *x*- and *y* directions, respectively. The effective mass of electron in

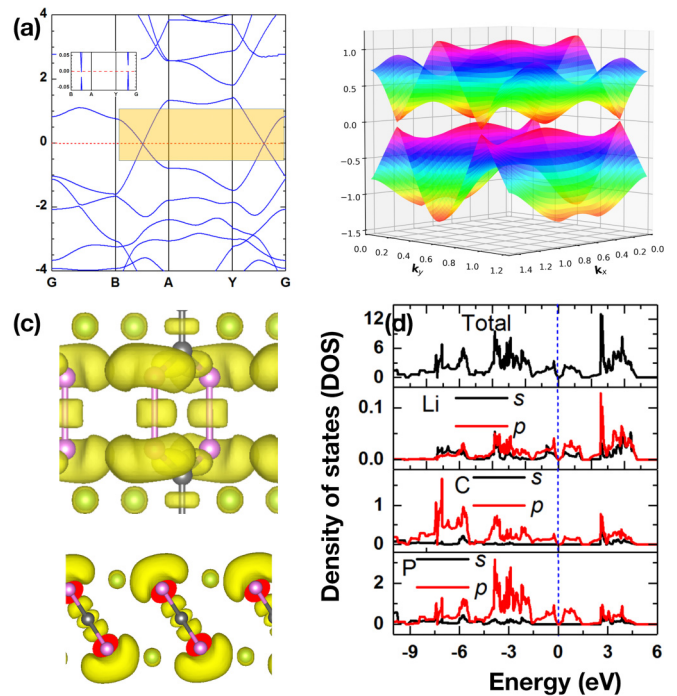


FIG. 6. Electronic properties of LiCP₂ monolayer: (a) Projected band structure; (b) three-dimensional band structures of the highest valence band and lowest conduction band; (c) ELF with isosurface value set to 0.8; and (d) total density of states DOS of LiCP₂, along with orbital projection for *p* and *s* orbitals of C, P, and Li.

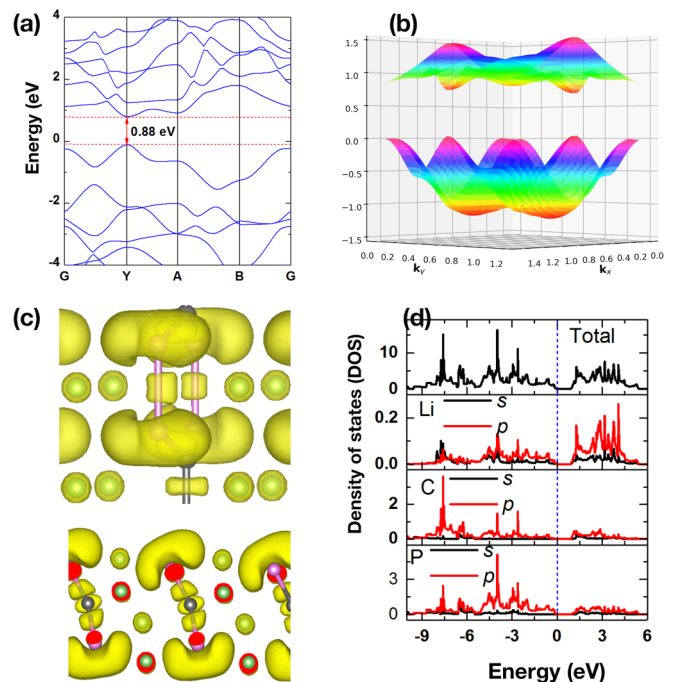


FIG. 7. Electronic properties of Li₂CP₂ monolayer: (a) Projected band structure; (b) three-dimensional band structures of the highest valence band and lowest conduction band; (c) ELF with isosurface value set to 0.65; and (d) total DOS of Li₂CP₂, along with orbital projection for *p* and *s* orbitals of C, P, and Li.

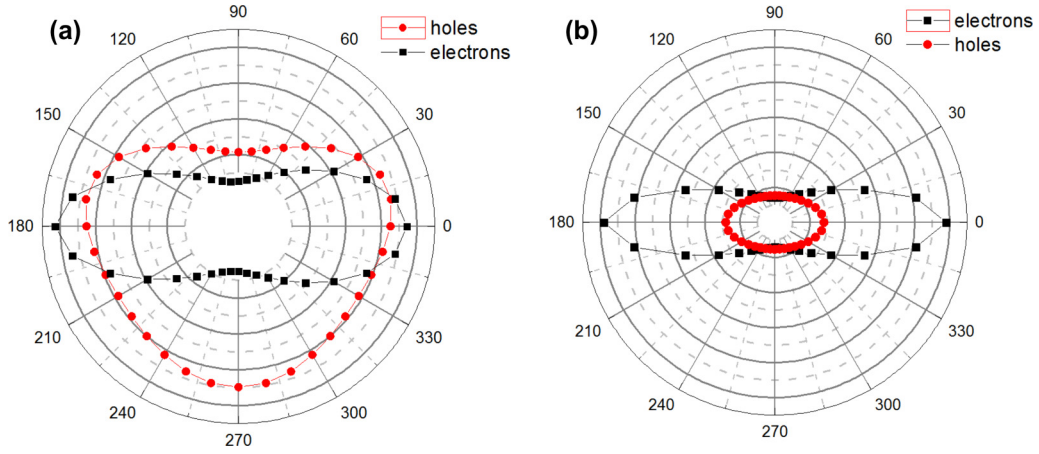


FIG. 8. Effective mass of electrons and holes of CP₂ (a) and Li₂CP₂ (b) along different directions at CBM and VBM; The magnitude of effective mass is proportional to distance from center to data point.

Li₂CP₂ along the y direction is $0.09 m_0$ less than that in CP₂. The effective mass of electron in Li₂CP₂ along the x direction is much higher than that in CP₂, which may be attributed to the breaking of P–P bonds due to the lithiation. The minimum effective mass of holes in Li₂CP₂ along the x - and y directions are $0.42 m_0$ and $0.23 m_0$, respectively.

The carrier mobility is calculated to understand the electronic conductance of CP₂ and Li₂CP₂. The carrier mobility μ_{2D} was calculated using the below expression based on the deformation potential theory [9,44,45]:

$$\mu_{2D} = \frac{e\hbar^3 C_{2D}}{k_B T m_e^* m_d (E_1^i)^2},$$

where e , \hbar , and T are electron charge, Planck's constant, and temperature, respectively; m_e^* is the effective mass of electron or holes in the transport direction, which can be calculated from the derivatives of electronic bands. $m_d = \sqrt{(m_x^* m_y^*)}$ is the average effective mass of electrons or holes. E_1^i is the deformation potential constant for electrons or holes, defined as $E_1^i = \Delta V_i \times \frac{l_0}{\Delta l}$, in which ΔV_i is the energy change of the valence-band minimum or conduction-band maximum under proper cell compression and dilatation (calculated using a step of 0.5%).

The calculated carrier mobility using deformation potential theory at room temperature ($T = 300$ K) for CP₂ and Li₂CP₂ are summarized in Table IV, and detailed information of VBM and CBM band energy is summarized in Figs. S21–S24. The predicted electron mobility in the CP₂ shows moderately

large and isotropic along the x - and y directions, namely $0.373 \sim 0.396$ and $0.367 \sim 0.386 \text{ m}^2 \text{ V}^{-1} \text{ s}^{-1}$, respectively. While the hole mobility is significantly anisotropic, the hole mobility along the x direction is $5.192 \sim 6.826 \text{ m}^2 \text{ V}^{-1} \text{ s}^{-1}$, which is nearly 13 times the values along the y direction. Such strong anisotropy in hole mobility indicates that the CP₂ is a promising candidate for anisotropic electronic devices. The extremely large value of hole mobility along the x direction in the CP₂ monolayer can be attributed to the small deformation potential (0.41 ± 0.028 eV). It has been reported that the monolayer black phosphorus has a high hole mobility of $1 \sim 2.1 \text{ m}^2 \text{ V}^{-1} \text{ s}^{-1}$; the predicted hole mobility in the CP₂ is about 3–5 times higher than the maximum value in monolayer black phosphorus [9].

The predicted electron mobility in the Li₂CP₂ (Table IV) is significantly anisotropic, namely $0.007 \sim 0.008 \text{ m}^2 \text{ V}^{-1} \text{ s}^{-1}$ along the x direction and $4.665 \sim 7.336 \text{ m}^2 \text{ V}^{-1} \text{ s}^{-1}$ along the y direction. The hole mobility also shows anisotropic features with hole mobility of $0.106 \sim 0.120$ and $1.906 \sim 2.103 \text{ m}^2 \text{ V}^{-1} \text{ s}^{-1}$ along x - and y directions, respectively. In general, the carrier mobility along the y direction is significantly higher than that along the x direction, which may arise from the anisotropic structural arrangement. As discussed above, the unique structure of Li₂CP₂ results in a relatively high elastic constant along the y direction. In addition, the Li atoms are almost collinear along the y direction, which may facilitate carrier transport, leading to low carrier effective mass along the y direction. The relatively high elastic constant and low carrier effective mass result in relatively high carrier mobility along the y direction.

TABLE IV. The predicted carrier mobility of CP₂ and Li₂CP₂.

		m_x/m_0	m_y/m_0	E_{1x} (eV)	E_{1y} (eV)	C_{x2D} (J m ⁻²)	C_{y2D} (J m ⁻²)	μ_{x2D} (m ² V ⁻¹ s ⁻¹)	μ_{y2D} (m ² V ⁻¹ s ⁻¹)
CP ₂	e	0.47	0.12	1.73 ± 0.029	4.29 ± 0.055	60.35	92.50	$0.373 \sim 0.396$	$0.367 \sim 0.386$
	h	0.43	0.21	0.41 ± 0.028	2.40 ± 0.005	60.35	92.50	$5.192 \sim 6.826$	$0.540 \sim 0.545$
Li ₂ CP ₂	e	1.47	0.21	4.82 ± 0.11	0.71 ± 0.08	63.61	128.72	$0.007 \sim 0.008$	$4.665 \sim 7.336$
	h	0.42	0.23	3.04 ± 0.094	1.50 ± 0.004	63.61	128.72	$0.106 \sim 0.120$	$1.906 \sim 2.103$

Both the CP₂ and Li₂CP₂ show significant anisotropy and high carrier mobility. The CP₂ has a maximum hole mobility of 5.192~6.826 m² V⁻¹ s⁻¹ along the *x* direction, and the Li₂CP₂ reaches maximum electron mobility of 4.665~7.336 m² V⁻¹ s⁻¹ along the *y* direction. The carrier mobility in the CP₂ and Li₂CP₂ is much higher than that in many 2D materials, such as phosphorene and MoS₂ monolayer [9,46]. The significant anisotropy and extremely high carrier mobility in CP₂ and Li₂CP₂ should be valuable in future applications in electronics and optoelectronics.

D. Optical properties

The CP₂ monolayer has a band gap of 1.14 eV, which is desirable for photovoltaic and optoelectronic applications. Hence, the optical absorbance of CP₂ monolayer was evaluated using the HSE06 functional. The optical absorbance of black phosphorene monolayer and MoS₂ monolayer were also calculated for comparison. For low-dimensional materials, the dielectric function may depend on the thickness of the vacuum layer. To avoid the thickness problem, the optical conductivity $\sigma_{2D}(\omega)$ is used to characterize the optical properties of 2D sheets. The 3D optical conductivity can be calculated using the following expression [47,48]:

$$\sigma_{3D}(\omega) = i[1 - \epsilon(\omega)]\epsilon_0\omega,$$

where $\epsilon(\omega)$ is a frequency-dependent complex dielectric function, ϵ_0 is the permittivity of vacuum, and ω is the frequency of incident wave. The in-plane 2D optical conductivity was calculated using the below expression [47,48]:

$$\sigma_{2D}(\omega) = L\sigma_{3D}(\omega),$$

where L is the slab thickness in the simulation cell. The normalized absorbance $A(\omega)$ can be calculated using the following expression [47,48]:

$$A = \frac{Re\tilde{\sigma}}{|1 + \tilde{\sigma}/2|^2},$$

where $\tilde{\sigma} = \sigma_{2D}(\omega)/\epsilon_0c$ is the normalized conductivity and c is the speed of light.

As shown in Fig. 9, the CP₂ exhibits strong light absorption over a broad range from 300 to 750 nm. There is a wide overlap area between the absorption spectrum and the solar flux in the UV- to visible-light range, indicating the extraordinary light-harvesting ability in the UV- to visible-light spectrum. The optical absorbance of CP₂ is significantly larger than that of monolayer black phosphorene from UV- to visible-light region. Among 2D materials, MoS₂ has shown strong light absorption in the visible region [49,50]. CP₂ also showed stronger light absorption compared to that of MoS₂ monolayer in the visible region. The excellent optical performance indicates monolayer CP₂ is a very promising material for efficient photovoltaic solar cells and optoelectronic devices.

As presented in Fig. 10, the optical absorbance of LiCP₂ is strong anisotropy, as the absorbance along the *y* direction is significantly higher than that along the *x* direction from the near-infrared to midwave-infrared region. The LiCP₂ exhibits two strong absorbance peaks located at ~2000 and ~3700 nm. The absorbance approaches extremely large val-

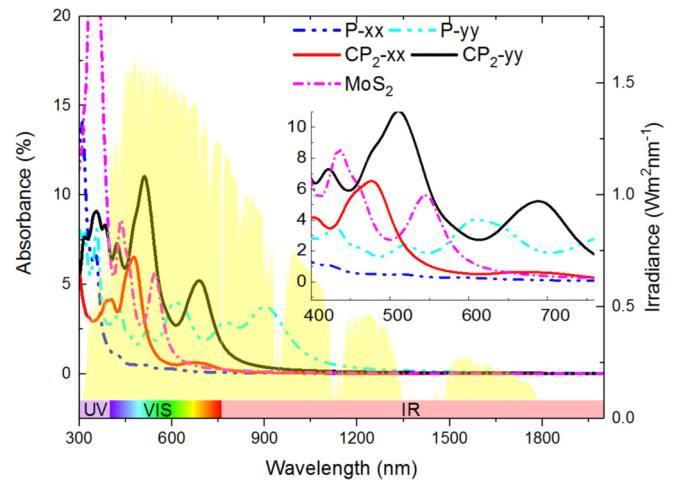


FIG. 9. Calculated in-plane absorption coefficients of CP₂ monolayers. The yellow background indicates the reference solar spectral irradiance (right y axis, air mass 1.5, ASTM G173-03).

ues up to 26%, indicating very strong light absorption in the midwave-infrared region. It is well known that optoelectronics in the midwave infrared is of paramount importance for applications including environmental monitoring, gas sensing, hazard detection, food and product manufacturing inspection, and so forth. The few-layer black phosphorus is reported as a promising 2D material for photodetection in the midwave-infrared spectral range [51]. Compared with monolayer black phosphorus, LiCP₂ shows stronger optical absorption in the midwave-infrared region, which makes it a promising and efficient medium-wave infrared optoelectronic material.

As shown in Fig. 11, the optical absorbance of Li₂CP₂ also shows strong anisotropy. The light absorbance of Li₂CP₂ along the *y* direction is significantly higher than that along the *x* direction in UV and 440~2000-nm region. The Li₂CP₂ exhibits strong light absorbance peaks at 650 and 760 nm. Compared with monolayer black phosphorus, Li₂CP₂ shows stronger light absorption in the near-infrared region, which

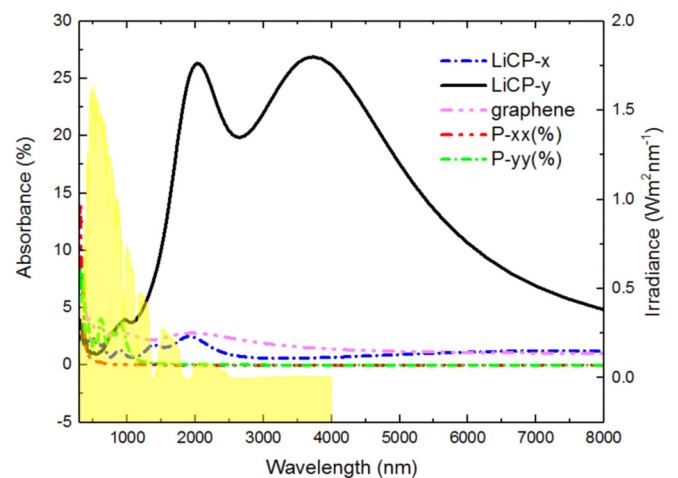


FIG. 10. Calculated in-plane absorption coefficients of LiCP₂ monolayers. The yellow background indicates the reference solar spectral irradiance (right y axis, air mass 1.5, ASTM G173-03).

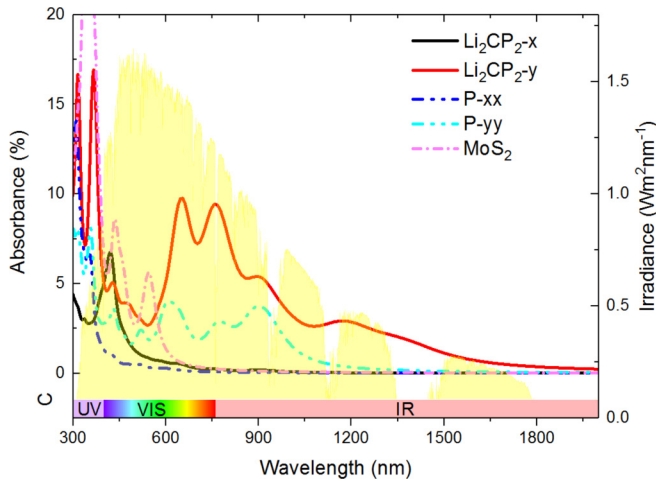


FIG. 11. Calculated in-plane absorption coefficients of Li_2CP_2 monolayers. The yellow background indicates the reference solar spectral irradiance (right y axis, air mass 1.5, ASTM G173-03).

means Li_2CP_2 monolayer has a broad application prospect in the near-infrared optical field.

Overall, all the three 2D materials CP_2 , LiCP_2 , and Li_2CP_2 are predicted to have anisotropic optical properties, which distinguishes them from other 2D materials, such as MoS_2 and graphene with isotropic optical properties. It should be noted that the optical absorbances of LiCP_2 and Li_2CP_2 along the y direction are significantly higher than that in the x direction. This may be attributed to the unique structural arrangement of LiCP_2 and Li_2CP_2 , in which the almost collinear arrangement of Li atoms along the y direction may benefit carrier transport with particularly low scattering, thus resulting in relatively high optical absorbance along the y direction. The excellent anisotropic optical feature makes them promising materials for nano-optical devices sensitive to polarized light. The CP_2 exhibits extraordinary light-harvesting ability in the UV- to visible-light region, which should be valuable in applications such as efficient photovoltaic solar cells and optoelectronic devices. The LiCP_2 shows very strong light

absorption in midwave-infrared regions, which is desirable for midwave-infrared optoelectronic devices, while the Li_2CP_2 shows strong optical absorbance in the near-infrared light region, which makes it a promising candidate for applications in near-infrared optoelectronics.

IV. CONCLUSION

In summary, two-dimensional CP_2 and Li_xCP_2 ($x = 1$ and 2) monolayer with a number of favorable functional properties has been proposed through density-functional theory calculations. The CP_2 is a semiconductor with an indirect band gap of 1.14 eV and high hole mobility of $5.192 \sim 6.826 \text{ m}^2 \text{ V}^{-1} \text{ s}^{-1}$ along the x direction and exhibits extraordinary light-harvesting ability in the UV- to visible-light region, which should be valuable in applications such as efficient photovoltaic solar cells and optoelectronic devices. More importantly, the lithiation of CP_2 induced the phase transformation of CP_2 to LiCP_2 or Li_2CP_2 , and the electronic properties change from indirect band-gap semiconductor to semimetal or direct band-gap semiconductor. Unlike CP_2 , LiCP_2 is a semimetal with Fermi velocities of up to $0.69 \times 10^6 \text{ m/s}$, comparable to that of graphene. Further increasing the Li concentration would lead to the formation of Li_2CP_2 , which is a semiconductor with a direct band gap of 0.88 eV and high electron mobility of $4.665 \sim 7.336 \text{ m}^2 \text{ V}^{-1} \text{ s}^{-1}$ along the y direction. The LiCP_2 and Li_2CP_2 exhibit high optical absorbance in midwave-infrared and near-infrared regions, respectively, which makes them promising candidates for applications in midwave-infrared and near-infrared optoelectronics.

ACKNOWLEDGMENTS

This work is supported by the National Natural Science Foundation of China (Grants No. 52071156, No. 51601068, No. 51625102, and No. 51471053), Natural Science Foundation of Fujian Province (Grant No. 2020J05147), and the Foundation from the Department of Science and Technology of Fujian Province (Grant No. 2019L3008).

- [1] M.-Q. Long, L. Tang, D. Wang, L. Wang, and Z. Shuai, *J. Am. Chem. Soc.* **131**, 17728 (2009).
- [2] X. Du, I. Skachko, A. Barker, and E. Y. Andrei, *Nat. Nanotechnol.* **3**, 491 (2008).
- [3] J.-H. Chen, C. Jang, S. Xiao, M. Ishigami, and M. S. Fuhrer, *Nat. Nanotechnol.* **3**, 206 (2008).
- [4] M. Orlita, C. Faugeras, P. Plochocka, P. Neugebauer, G. Martinez, D. K. Maude, A.-L. Barra, M. Sprinkle, C. Berger, W. A. de Heer, and M. Potemski, *Phys. Rev. Lett.* **101**, 267601 (2008).
- [5] X. Xu, C. Liu, Z. Sun, T. Cao, Z. Zhang, E. Wang, Z. Liu, and K. Liu, *Chem. Soc. Rev.* **47**, 3059 (2018).
- [6] Y. Zhang, T. Tang, C. Girit, Z. Hao, M. C. Martin, A. Zettl, M. F. Crommie, Y. R. Shen, and F. Wang, *Nature (London)* **459**, 820 (2009).
- [7] S. Zhou, G. H. Gweon, A. V. Fedorov, P. N. First, W. A. De Heer, D. H. Lee, F. Guinea, A. H. C. Neto, and A. Lanzara, *Nat. Mater.* **6**, 770 (2007).
- [8] R. Balog, B. Jorgensen, L. Nilsson, M. Andersen, E. Rienks, M. Bianchi, Z. Sljivancanin, F. Besenbacher, B. Hammer, T. G. Pedersen, P. Hofmann, and L. Hornekær, *Nat. Mater.* **9**, 315 (2010).
- [9] J. Qiao, X. Kong, Z.-X. Hu, F. Yang, and W. Ji, *Nat. Commun.* **5**, 4475 (2014).
- [10] L. Li, Y. Yu, G. J. Ye, Q. Ge, X. Ou, H. Wu, D. Feng, X. H. Chen, and Y. Zhang, *Nat. Nanotechnol.* **9**, 372 (2014).
- [11] L. Li, J. Kim, C. Jin, G. J. Ye, D. Y. Qiu, F. H. da Jornada, Z. Shi, L. Chen, Z. Zhang, F. Yang *et al.*, *Nat. Nanotechnol.* **12**, 21 (2017).
- [12] G. Wang, R. Pandey, and S. P. Karna, *Nanoscale* **8**, 8819 (2016).

- [13] J. Guan, D. Liu, Z. Zhu, and D. Tománek, *Nano Lett.* **16**, 3247 (2016).
- [14] B. Rajbanshi and P. Sarkar, *J. Phys. Chem. Lett.* **8**, 747 (2017).
- [15] S. A. Shcherbinin, K. Zhou, S. V. Dmitriev, E. A. Korznikova, A. R. Davletshin, and A. A. Kistanov, *J. Phys. Chem. C* **124**, 10235 (2020).
- [16] T. Yu, Z. Zhao, Y. Sun, A. Bergara, J. Lin, S. Zhang, H. Xu, L. Zhang, G. Yang, and Y. Liu, *J. Am. Chem. Soc.* **141**, 1599 (2019).
- [17] M. Kar, R. Sarkar, S. Pal, and P. Sarkar, *Phys. Rev. B* **101**, 195305 (2020).
- [18] M. T. Kuo, P. W. May, A. Gunn, M. N. R. Ashfold, and R. K. Wild, *Diamond Relat. Mater.* **9**, 1222 (2000).
- [19] S. R. J. Pearce, P. W. May, R. K. Wild, K. R. Hallam, and P. J. Heard, *Diamond Relat. Mater.* **11**, 1041 (2002).
- [20] F. Claeysens, G. M. Fuge, N. L. Allan, P. W. May, and M. N. R. Ashfold, *Dalton Trans.* **19**, 3085 (2004).
- [21] J. N. Hart, P. W. May, N. L. Allan, K. R. Hallam, F. Claeysens, G. M. Fuge, M. Ruda, and P. J. Heard, *J. Solid State Chem.* **198**, 466 (2013).
- [22] A. Furlan, G. K. Gueorguiev, Z. Czigány, H. Högberg, S. Braun, S. Stafström, and L. Hultman, *Physica Status Solidi RRL* **2**, 191 (2008).
- [23] W. C. Tan, Y. Cai, R. J. Ng, L. Huang, X. Feng, G. Zhang, Y.-W. Zhang, C. A. Nijhuis, X. Liu, and K.-W. Ang, *Adv. Mater.* **29**, 1700503 (2017).
- [24] W. C. Tan, L. Huang, R. J. Ng, L. Wang, D. M. N. Hasan, T. J. Duffin, K. S. Kumar, C. A. Nijhuis, C. Lee, and K.-W. Ang, *Adv. Mater.* **30**, 1705039 (2018).
- [25] M. Mayo, K. J. Griffith, C. J. Pickard, and A. J. Morris, *Chem. Mater.* **28**, 2011 (2016).
- [26] W. Zhang, J. Yin, P. Zhang, X. Tang, and Y. Ding, *J. Mater. Chem. A* **6**, 12029 (2018).
- [27] P. E. Blöchl, *Phys. Rev. B* **50**, 17953 (1994).
- [28] G. Kresse and J. Furthmüller, *Phys. Rev. B* **54**, 11169 (1996).
- [29] J. P. Perdew, K. Burke, and M. Ernzerhof, *Phys. Rev. Lett.* **77**, 3865 (1996).
- [30] J. P. Perdew, K. Burke, and Y. Wang, *Phys. Rev. B* **54**, 16533 (1996).
- [31] S. Grimme, J. Antony, S. Ehrlich, and H. Krieg, *J. Chem. Phys.* **132**, 154104 (2010).
- [32] J. Paier, M. Marsman, K. Hummer, G. Kresse, I. C. Gerber, and J. G. Ángyán, *J. Chem. Phys.* **124**, 154709 (2006).
- [33] K. Parlinski, Z. Q. Li, and Y. Kawazoe, *Phys. Rev. Lett.* **78**, 4063 (1997).
- [34] G. Henkelman, B. P. Uberuaga, and H. Jónsson, *J. Chem. Phys.* **113**, 9901 (2000).
- [35] V. Wang, N. Xu, J.-C. Liu, G. Tang, and W.-T. Geng, *Comput. Phys. Commun.* **267**, 108033 (2021).
- [36] S. Maintz, V. L. Deringer, A. L. Tchougréeff, and R. Dronskowski, *J. Comput. Chem.* **34**, 2557 (2013).
- [37] S. Maintz, V. L. Deringer, A. L. Tchougréeff, and R. Dronskowski, *J. Comput. Chem.* **37**, 1030 (2016).
- [38] See Supplemental Material at <http://link.aps.org/supplemental/10.1103/PhysRevB.106.075402> for formation energies of Li_xCP₂, phonon dispersion of NaCP₂ and KCP₂, and band energy of the CBM and VBM of CP₂.
- [39] Y. Le Page and P. Saxe, *Phys. Rev. B* **63**, 174103 (2001).
- [40] A. Jain, S. P. Ong, G. Hautier, W. Chen, W. D. Richards, S. Dacek, S. Cholia, D. Gunter, D. Skinner, G. Ceder, and K. A. Persson, *APL Mater.* **1**, 011002 (2013).
- [41] S. Zhao, W. Kang, and J. Xue, *J. Mater. Chem. A* **2**, 19046 (2014).
- [42] P. E. Trevisanutto, C. Giorgetti, L. Reining, M. Ladisa, and V. Olevano, *Phys. Rev. Lett.* **101**, 226405 (2008).
- [43] L. D. Whalley, J. M. Frost, B. J. Morgan, and A. Walsh, *Phys. Rev. B* **99**, 085207 (2019).
- [44] R. Fei and L. Yang, *Nano Lett.* **14**, 2884 (2014).
- [45] S. Bruzzone and G. Fiori, *Appl. Phys. Lett.* **99**, 222108 (2011).
- [46] B. Radisavljevic, A. Radenovic, J. Brivio, V. Giacometti, and A. Kis, *Nat. Nanotechnol.* **6**, 147 (2011).
- [47] L. Matthes, O. Pulci, and F. Bechstedt, *New J. Phys.* **16**, 105007 (2014).
- [48] L. Matthes, O. Pulci, and F. Bechstedt, *Phys. Rev. B* **94**, 205408 (2016).
- [49] O. Lopez-Sanchez, D. Lembke, M. Kayci, A. Radenovic, and A. Kis, *Nat. Nanotechnol.* **8**, 497 (2013).
- [50] H. Wang, C. Zhang, W. Chan, S. Tiwari, and F. Rana, *Nat. Commun.* **6**, 8831 (2015).
- [51] N. Youngblood, C. Chen, S. J. Koester, and M. Li, *Nat. Photonics* **9**, 247 (2015).